Efficient Convex Optimization Approaches to Variational Image Fusion

Jing Yuan[1], Brandon Miles[1], Juan Shi[3], Greg Garvin[2], Xue-Cheng Tai[3,4], and Aaron Fenster[1]

[1] Medical Imaging Lab, Robarts Research Institute, University of Western Ontario
London, Ontario, Canada N6A 5B7
cn.yuanjing@gmail.com, bmiles@uwo.ca, afenster@imaging.robarts.ca
[2] Department of Medical Imaging, St Jospeh's HealthCare
London, Ontario, Canada
Greg.Garvin@lhsc.on.ca
[3] Division of Mathematical Sciences, School of Phys. and Math. Sci.
Nanyang Technological University, Singapore
shij0004@e.ntu.edu.sg
[4] Department of Mathematics, University of Bergen
Bergen, Norway tai@mi.uib.no

Abstract. Image fusion is an imaging technique to visualize information from multiple imaging sources by one single image, which is widely used in remote sensing, medical imaging etc. In this work, we study two variational approaches to image fusion which are closely related to the standard TV-L_2 and TV-L_1 image approximation methods. We investigate their convex optimization formulations, under the perspective of primal and dual, and propose their associated new image decomposition models. In addition, we consider the TV-L_1 based image fusion approach and study the specified problem of fusing two discrete-constrained images $f_1(x) \in \mathcal{L}_1$ and $f_2(x) \in \mathcal{L}_2$, where $\mathcal{L}_1$ and $\mathcal{L}_2$ are the sets of linearly-ordered discrete values. We prove that the TV-L_1 based image fusion actually gives rise to the exact convex relaxation to the corresponding nonconvex image fusion constrained by the discrete-valued set $u(x) \in \mathcal{L}_1 \cup \mathcal{L}_2$. This extends the results for the global optimization of the discrete-constrained TV-L_1 image approximation [7, 33] to the case of image fusion. As a big numerical advantage of the two proposed dual models, we show both of them directly lead to new fast and reliable algorithms, based on modern convex optimization techniques. Experiments of medical imaging, remote sensing and multi-focusing visibly show the qualitive differences between the two studied variational models of image fusion. We also apply the new variational approaches to fusing 3D medical images.

1 Introduction

Imaging fusion technologies have been developed to be an effective way to show different imagery information, acquired through various sources, in one single

image, which is interesting in many areas, e.g. remote sensing [27, 10], medical imaging [25, 29] and synthesis of multi-focused images [16, 26]. More specifically, given two or more imaging data which are from different information sources and properly aligned, image fusion integrates all such data into one visualized image, mostly with higher spatial or spectral resolution. For example, two images may capture the same scene but with different focuses (see the left two images of Fig. 1), fusing these two images clearly gives a better visual result (see the right two fused images of Fig. 1). In remote sensing and satellite imaging, the fused image, which is merged by multispectral data, effectively carries much more information [27, 24]. In medical imaging, while both the Magnetic Resonance (MR) and Computed Tomography (CT) imagery provide standard diagnostic tools other than fluoroscopy and ultrasound techniques, it is well-known that a CT scan will adequately highlight the bone structure details while soft tissue information is not clearly visible; on the other hand, a T2 weighted MR scan produces significantly better details for images of these tissues. In this respect, it is highly desirable to have a combined view of CT and MR images, which illustrates significant details both from both CT and MR inputs and assists clinical diagnoses.

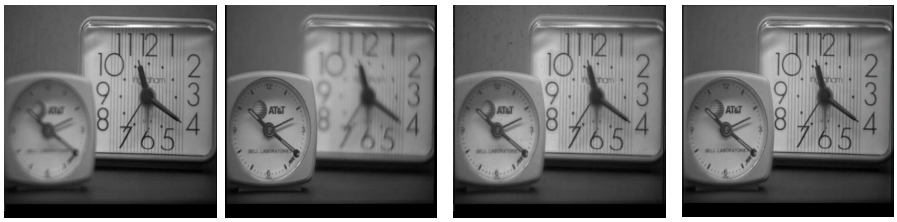

(a) (b) (c) (d)

Fig. 1. Multi-focus image fusion: (a) and (b) give two images exposed with different focuses; (c) and (d) are the fused image computed by the proposed methods (1) and (3) in this work.

Parallel to the recent developments of image processing, many pixelwise image fusion methods have been proposed to tackle the issues of combining multiple images or informative data, e.g. the wavelet or contourlet based approaches [20, 18, 29], high-pass filtering method [1, 24] etc. In this paper, we concentrate on the variational approaches to image fusion, which were explored in [21, 26, 15]. Energy minimization and variational methods have been developed to be a standard way to effectively and reliably handle many practical topics of image processing and computer vision. Successful applications include image denoising and restoration [23, 8, 33, 19, 28], image decomposition [2, 17, 30] and image segmentation [9, 8, 32, 31] etc. With respect to this, the total-variational based image fusion methods [26, 15] provide such an elegant approach in theory for

the tradeoff between redundant imagery information and image priors. In this paper, we propose the novel convex optimization approaches to the variational models under the novel duality-based perspective. We consider, in particular, the exactness of the reduced convex relaxation model to the nonconvex TV-L1 based image fusion with the pixelwise constraint of discrete values. We show that the proposed dual models directly lead to new fast and reliable algorithms in numerics, which can be easily implemented and speeded up by the modern paralell computing platforms, e.g. GPU.

1.1 Contributions

We summarize our contributions as follows:

- We study the convex optimization model of image fusion based on standard technique of TV-L_2 image approximation and extend it to the TV-L_1 based image fusion model. We propose their novel equivalent convex formulations under the perspective of primal and dual. We show the studied image fusion models actually result in two new image decompositions of the weighted input image, with helps of the proposed new dual forumations.

- In addition, we prove the TV-L_1 based image fusion method actually gives an exact convex relaxation model to the corresponding image fusion problem constrained by a linearly-ordered discrete-value set to each pixel, i.e. it solves such nonconvex image fusion problem globally and exactly. This result properly extends the convex relaxation models of TV-L1 image approximation, proposed by Chan et al [7] and Yuan et al [33], to the application of TV-L1 based image fusion.

  On the other hand, direct and global solvers to such discrete-constrained image fusion, especially over a large number of linearly-ordered discrete values in medical imaging, definitely result in a high load of memory and computation and make them inapplicable in practice, e.g. graph-cuts method [5, 14] and the continuous min-cut method [3]. To this end, the convex relaxation approach proposed in this work leads to a much more efficient and reliable way to tackle the studied discrete-constrained optimization problem, with much lower memory load.

- We also derive fast multiplier-based algorithms to the studied two image fusion methods directly through the proposed dual formulations. In numerics, the algorithms avoid nonsmoothness of the energy functions and lead to simple and efficient numerical implementations. We demonstrate their numerical performances with both CPU and GPU.

2 Convex Optimization Models

Given two input images $f_1(x)$ and $f_2(x)$, a total-variation based method for image fusion was proposed by Wang et al [26] such that

$$\min_{u\in BV(\Omega)} \frac{1}{2}\int_\Omega w_1\,(u-f_1)^2\,dx + \frac{1}{2}\int_\Omega w_2\,(u-f_2)^2\,dx + \alpha\int_\Omega |\nabla u|\,dx \quad (1)$$

where the functions $\omega_1(x)$ and $\omega_2(x)$ are the pixelwise weight functions such that

$$\omega_1(x)+\omega_2(x) = 1\,, \quad \omega_{1,2}(x)\geq 0\,; \quad \forall x\in\Omega\,. \quad (2)$$

In this work, we extend (1) to the convex optimization model with the L_1-normed data fidelity term:

$$\min_u \int_\Omega w_1\,|u-f_1|\,dx + \int_\Omega w_2\,|u-f_2|\,dx + \alpha\int_\Omega |\nabla u|\,dx\,. \quad (3)$$

Similar formulation as (3) was also studied in [15] where the weight functions are given constant.

Clearly, both models (1) and (3) formulate the integration of two input images as the problem of convex optimization which can be generalized as follows

$$\min_u \int_\Omega w_1 D_1(f_1-u)\,dx + \int_\Omega w_2 D_2(f_2-u)\,dx + \alpha\int_\Omega |\nabla u|\,dx \quad (4)$$

where $D_1(\cdot)$ and $D_2(\cdot)$ are positive convex functions. In this work, we call (4), along with (1) and (3), the *primal model*.

In the following parts, we investigate (4) under the perspective of primal and dual and build up its connections to variational image decomposition.

2.1 Equivalent Convex Formulations

Let $D_1^*(q)$ and $D_2^*(q)$ be the respective conjugate of the convex function $D_1(v)$ and $D_2(v)$ such that

$$D_1(v) = \max_{q_1}\{vq_1 - D_1^*(q_1)\}\,, \quad D_2(v) = \max_{q_2}\{vq_2 - D_2^*(q_2)\}\,. \quad (5)$$

For the model (1) where the functions D_1 and D_2 are in quadratic forms, i.e. $D_1(v) = D_2(v) = \frac{1}{2}v^2$, we have

$$D_1^*(q) = D_2^*(q) = \frac{1}{2}q^2\,. \quad (6)$$

For the problem (3) where both D_1 and D_2 are absolute functions, i.e. $D_1(v) = D_2(v) = |v|$, we have

$$D_1^*(q) = D_2^*(q) = I_\delta(q\in[-1,1]) \quad (7)$$

where $I_\delta(q \in [-1,1])$ is the characteristic function of the convex set $q \in [-1,1]$.

We also recall that the dual formulation of the total-variation function [13]

$$\alpha \int_\Omega |\nabla u| \, dx \, = \, \max_{p \in C_\alpha} \int_\Omega u \, \mathrm{div}\, p \, dx \tag{8}$$

where C_α is a convex set defined by

$$C_\alpha \, := \, \{ p \, | \, p \in C_c^1(\Omega, \mathbb{R}^2) \, , \; |p(x)| \leq \alpha \, , \; \forall x \in \Omega \, \} \, . \tag{9}$$

By simple computation, in view of (5) and (8), the generalized problem (4) can be equally rewritten as

$$\begin{aligned} \min_u \max_{q_1, q_2} \max_{p \in C_\alpha} & \int_\Omega w_1 \, (q_1 f_1 - D_1^*(q_1)) \, dx \, + \, \int_\Omega w_2 \, (q_2 f_2 - D_2^*(q_2)) \, dx \\ & + \, \langle \mathrm{div}\, p - (w_1 q_1 + w_2 q_2), u \rangle \, . \end{aligned} \tag{10}$$

In this paper, we call (10) the equivalent *primal-dual model* of (4).

Observe that u is unconstrained and the convex formulation (10) suffices the minimax theorem [11, 12] for our cases (1) and (3) in this study, the min and max operators of (10) are interchangeable. The minimization of (10) over u, therefore, leads to the linear equality

$$w_1 q_1 \, + \, w_2 q_2 \, = \, \mathrm{div}\, p \, , \tag{11}$$

and the corresponding linear-equality constrained maximization problem:

$$\begin{aligned} \max_{q_1, q_2} \max_{p \in C_\alpha} & \int_\Omega w_1 \, (q_1 f_1 - D_1^*(q_1)) \, dx \, + \, \int_\Omega w_2 \, (q_2 f_2 - D_2^*(q_2)) \, dx \\ \text{s.t.} \quad & w_1 q_1 \, + \, w_2 q_2 \, = \, \mathrm{div}\, p \, . \end{aligned} \tag{12}$$

Similarly, we call (12) the equivalent *dual model* of (4).

2.2 Variational Image Decompositions

With helps of the conjugates (5), we will see that the optimum of the generalized image fusion model (4) actually proposes the decomposition of the weighted input image $f(x) := (w_1 \, f_1 + w_2 \, f_2)(x)$, $\forall x \in \Omega$, such that

Proposition 1. *Given the optimal primal-dual pair (q_1^*, q_2^*, p^*, u^*) to the primal-dual model* (10)*, (q_1^*, q_2^*, p^*, u^*) just gives rise to the decomposition of the weighted input image $(w_1 f_1 + w_2 f_2)(x)$, $\forall x \in \Omega$, as follows*

$$f \, (:= \, w_1 f_1 + w_2 f_2 \,) \, = \, u^* + v^* \tag{13}$$

where

$$v^* \, = \, w_1 v_1^* + w_2 v_2^* \, , \quad v_1^* \in \partial D_1(q_1^*) \, , \; v_2^* \in \partial D_2(q_2^*) \, .$$

Proof. Observe the conjugate formulations (5), we have

$$f_1 - u^* \,=\, v_1^* \,\in\, \partial D_1(q_1^*)\,, \quad f_2 - u^* \,=\, v_2^* \,\in\, \partial D_2(q_2^*)\,.$$

Recall that $w_1(x) + w_2(x) = 1$ for $\forall x \in \Omega$, then we have

$$w_1 v_1^* + w_2 v_2^* \,=\, w_1(f_1 - u^*) + w_2(f_2 - u^*) \,=\, (w_1 f_1 + w_2 f_2) - u^*\,.$$

Then (13) simply follows.

Image Decomposition by TV-L_2 Image Fusion (1) Consider the conjugates (6) and Prop. 1, the TV-L_2 based image fusion problem (1) results in the following image decomposition:

Corollary 1 *Given the optimal prima-dual pair (q_1^*, q_2^*, p^*, u^*) to the equivalent primal-dual model* (10) *associated to* (1)*, (q_1^*, q_2^*, p^*, u^*) just gives rise to the decomposition of the weighted input image $(w_1 f_1 + w_2 f_2)(x)$, $\forall x \in \Omega$, such that*

$$f\,(:=\, w_1 f_1 + w_2 f_2\,) \,=\, u^* + \operatorname{div} p^*\,. \tag{14}$$

Proof. In view of (6), we have

$$f_1 - u^* \,=\, q_1^*\,, \quad f_2 - u^* \,=\, q_2^*\,.$$

Therefore, it follows that

$$f \,:=\, w_1 f_1 + w_2 f_2 \,=\, (w_1 q_1 + w_2 q_2) + u^*\,.$$

In view of the linear equality constraint (11), i.e. $w_1 q_1^* + w_2 q_2^* \,=\, \operatorname{div} p^*$, then we have

$$f \,:=\, w_1 f_1 + w_2 f_2 \,=\, u^* + \operatorname{div} p^*\,.$$

Consequentlly, we have

Corollary 2 *The image fusion problem* (1) *is equivalent to*

$$\min_{p \in C_\alpha} \,\left\| (w_1 f_1 + w_2 f_2) - \operatorname{div} p \right\|^2\,, \tag{15}$$

i.e. the projection of the weighted input image $(w_1 f_1 + w_2 f_2)(x)$, $x \in \Omega$, to the convex set $\operatorname{div} C_\alpha$*.*

Proof directly follows from the image decomposition model of Coro. 1 and (6).

Clearly, the results of Coro. 1 and Coro. 2 are similar to the image decomposition and projection formulations derived from TV-L_2 image approximation proposed in [6, 2].

Image Decomposition by TV-L_1 Image Fusion (3) Likely, the TV-L_1 based image fusion model (3) results in image decomposition as follows:

Corollary 3 *Given the optimum* (q_1^*, q_2^*, p^*, u^*) *of the equivalent primal-dual model* (10) *which is equivalent to* (3), (q_1^*, q_2^*, p^*, u^*) *just gives rise to the decomposition of the weighted input image* $(w_1 f_1 + w_2 f_2)(x)$, $x \in \Omega$, *such that*

$$f \,:=\, w_1 f_1 + w_2 f_2 \,=\, u^* + v^* \tag{16}$$

where

$$v^* \,=\, w_1 v_1^* + w_2 v_2^* \,, \quad v_1^* \in \partial I_S(q_1^*) \,,\; v_2^* \in \partial I_S(q_2^*) \,,$$

I_S *is the characteristic function of the set* $S = \{q \,|\, q(x) \in [-1, 1] \,,\; \forall x \in \Omega \,\}$.

Its proof directly follows by the conjugates (7) and Prop. 1.

3 Global and Exact Optimization

Now we focus on the TV-L_1 based approach (3); in particular, we consider the specified discrete-valued non-convex optimization problem

$$\min_{u(x) \in \mathcal{L}} \int_\Omega w_1 \,|u - f_1| \; dx \,+\, \int_\Omega w_2 \,|u - f_2| \; dx \,+\, \alpha \int_\Omega |\nabla u| \; dx \tag{17}$$

where we assume the two input images $f_1(x)$ and $f_2(x)$ take discrete values which are linearly ordered such that

$$f_i(x) \,\in\, \mathcal{L}_i \,\left(:= \{l_1^i, \ldots, l_{n_i}^i\}\right) \,, \quad l_1^i < l_2^i < \ldots < l_{n_i}^i \,; \quad i \,=\, 1 \,, 2 \tag{18}$$

and $\mathcal{L} = \mathcal{L}_1 \cup \mathcal{L}_2$ is the combination set of $\mathcal{L}_1$ and $\mathcal{L}_2$. In this regard, we also assume the set $\mathcal{L}$ includes n discrete values which is linearly ordered such that

$$\mathcal{L} \,=\, \{l_1, \ldots, l_n\} \,, \quad l_1 < l_2 < \ldots < l_n \,. \tag{19}$$

We show that the TV-L_1 based image fusion problem (3) amounts to the exact convex relaxation model of the above integer-constrained non-convex optimization problem (17), i.e. the optimum of the convex optimization problem (3) results in the global and exact integer-valued optimum of (17). A similar result was recently proposed by [33], where the authors proved that the convex TV-L_1 image approximation does give global and exact optima to the corresponding discrete-constrained TV-L_1 approximation.

To this end, we define the γ-upper level set U^γ of the given function $u(x)$, for each constantγ, as follows:

$$U^\gamma(x) \,=\, \begin{cases} 1 \,, & \text{when } u(x) > \gamma \\ 0 \,, & \text{when } u(x) \leq \gamma \end{cases} \,, \quad x \in \Omega \,. \tag{20}$$

Then we directly state our result as the following proposition.

Proposition 4 (Threshholding Rule) *Given the optimum $u^*(x)$ to* (3) *and the set of discrete values $\mathcal{L} = \{l_1, \ldots, l_n\}$, $l_1 < \ldots < l_n$, which is the combination of two sets* (18) *of discrete image values given in $f_1(x)$ and $f_2(x)$, then for any given $n-1$ values γ_i, $i = 1, \ldots, n-1$, such that*

$$l_1 < \gamma_1 < l_2 < \ldots < \gamma_{n-1} < l_n \,, \tag{21}$$

we define the image function $u^\gamma(x)$ by the $n-1$ upper level sets of $u^*(x)$:

$$u^\gamma(x) \;=\; l_1 + \sum_{i=1}^{n-1} (l_{i+1} - l_i)\, U^{\gamma_i}(x) \,. \tag{22}$$

where $U^{\gamma_i}(x)$ is defined by (20)*. Therefore, $u^\gamma(x) \in \mathcal{L}\,(:= \{l_1, \ldots, l_n\})$ gives an exact and global optimum of* (17)*.*

The detailed proof can be derived by the same way as [33] and includes a sequence of propositions as follows:

Proposition 5 (Extremum Principle) *Given the image functions $f_i(x) \in \mathcal{L}_i$, $i = 1, 2$, as* (18) *and the set $\mathcal{L}$ of discrete values as* (19)*, each minimum $u^*(x)$ of* (3) *suffices $l_1 \leq u^*(x) \leq l_n$, almost everywhere of Ω.*

The proof of Prop. 5 directly follows from the coarea theorem of the total-variation function and the facts:

$$l_1 \;\leq\; \min(l_1^1, l_1^2) \,, \quad l_n \;\geq\; \max(l_{n_1}^1, l_{n_2}^2) \,.$$

Proposition 6 *Given a bounded scalar function $l_1 \leq u(x) \leq l_n$, $\forall x \in \Omega$, if an optimal vector field p^* maximizes the integral $\int_\Omega u \operatorname{div} p \, dx$ over the convex set $p \in C_\alpha$ of* (9)*, i.e.*

$$\int_\Omega |\nabla u| \, dx \;=\; \int_\Omega u \operatorname{div} p^* \, dx \,,$$

then in view of (20)*, for every $\gamma-$upper level set $U^\gamma(x)$ of $u(x)$ with $\gamma \in [f_1, f_m)$, p^* also maximizes the integral $\int_\Omega U^\gamma \operatorname{div} p \, dx$ over the convex set $p \in C_\alpha$ and*

$$\int_\Omega U^\gamma \operatorname{div} p^* \, dx \;=\; |\partial U^\gamma| \,,$$

which gives the perimeter of the level set $U^\gamma(x)$.

The proof of Prop. 6 is given in [33].

Proposition 7 *Given a bounded scalar function $l_1 \leq u(x) \leq l_n$, $\forall x \in \Omega$, and $n-1$ different values γ_i, $i = 1, \ldots, n-1$, such that $l_1 \leq \gamma_1 < \ldots < \gamma_{n-1} \leq l_n$, if an optimal vector field p^* maximizes the integral $\int_\Omega u \operatorname{div} p \, dx$ over the convex set $p \in C_\alpha$, then for the image function*

$$u^\gamma(x) \;=\; l_1 \;+\; \sum_{i=1}^{n-1} (l_{i+1} - l_i)\, U^{\gamma_i}(x) \,,$$

p^* also maximizes the integral $\int_\Omega u^\gamma \operatorname{div} p\, dx$ over the convex set $p \in C_\alpha$, i.e.

$$\int_\Omega |\nabla u^\gamma|\, dx \;=\; \int_\Omega u^\gamma \operatorname{div} p^*\, dx\,.$$

The proof of Prop. 7 is given in [33].

4 Duality Based Algorithms

In this section, we propose fast numerical algorithms to image fusion problems (1) and (3) through their respective dual formulations.

Projection Algorithm to TV-L_2 Image Fusion (1) By Coro. 2, we observe that the image fusion problem (1) corresponds to the projection of the image $w_1 f_1 + w_2 f_2$ to the convex set $\operatorname{div} C_\alpha$. It directly leads to the same duality-based algorithm as [6] proposed by Chambolle. We list its iterative projected-gradient descent steps for computing the dual variable p as follows:

$$p^{i+1} \;=\; \mathbf{Proj}_{C_\alpha}\Big(p^i + \tau\nabla\big((w_1 f_1 + w_2 f_2) - \operatorname{div} p^i\big)\Big)\,,$$

where $\tau > 0$ gives the step-size at each iteration.

Multiplier-Based Algorithm to TV-L_1 Image Fusion (3) With helps of (7) and (10), the TV-L_1 based image fusion problem (3) can be equally written as the following primal-dual formulation:

$$\min_{u}\max_{q_1,q_2}\max_{p\in C_\alpha} \int_\Omega q_1 f_1\, dx \;+\; \int_\Omega q_2 f_2\, dx \;+\; \langle \operatorname{div} p - (q_1+q_2), u\rangle \tag{23}$$

$$\text{s.t.}\;\; q_1(x) \in [-w_1(x), w_1(x)]\,, \quad q_2(x) \in [-w_2(x), w_2(x)]\,. \tag{24}$$

Also in view of (12), its equivalent dual model can be formulated as

$$\max_{q_1,q_2}\max_{p\in C_\alpha} \int_\Omega q_1 f_1\, dx \;+\; \int_\Omega q_2 f_2\, dx \tag{25}$$

$$\text{s.t.}\;\; q_1(x) \in [-w_1(x), w_1(x)]\,, \quad q_2(x) \in [-w_2(x), w_2(x)]$$

$$q_1 + q_2 \;=\; \operatorname{div} p\,. \tag{26}$$

We see that the image $u(x)$ in the primal-dual formulation (23), which is what we wish to obtain, just works as the multiplier function to the linear equality constraint (26) of the dual model (25). In addition, the energy function of (23) gives the corresponding Lagrangian function to the dual formulation (25). Through these observations, we define its augmented Lagrangian function as

$$L_c(q_1, q_2, p, u) \;=\; \langle q_1, f_1\rangle + \langle q_2, f_2\rangle + \langle \operatorname{div} p - (q_1+q_2), u\rangle - \frac{c}{2}\left\|\operatorname{div} p - (q_1+q_2)\right\|^2$$

where $c > 0$.

In this work, we apply the classical augmented Lagrangian algorithm [22, 4] through its augmented Lagrangian function $L_c(q_1, q_2, p, u)$, which includes the following steps at k-th iteration:

1. Optimize q_1^{k+1} by fixing q_2^k, p^k and u^k, which gives

$$q_1^{k+1} := \underset{|q_1(x)|\leq w_1(x)}{\arg\max} \langle q_1, f_1\rangle - \frac{c}{2}\left\|q_1 - (\operatorname{div} p^k - q_2^k - u^k/c)\right\|^2 .$$

   It can be computed by the following step in a close form:

$$q_1^{k+1} = \operatorname{Proj}_{|q_1(x)|\leq w_1(x)}(f_1/c + (\operatorname{div} p^k - q_2^k(x) - u^k/c)) ; \tag{27}$$

2. Optimize q_2^{k+1} by fixing q_1^{k+1}, p^k and u^k, which gives

$$q_2^{k+1} := \underset{|q_2(x)|\leq w_2(x)}{\arg\max} \langle q_2, f_2\rangle - \frac{c}{2}\left\|q_2 - (\operatorname{div} p^k - q_1^{k+1} - u^k/c)\right\|^2 .$$

   It can be computed by the following step in a close form:

$$q_2^{k+1} = \operatorname{Proj}_{|q_2(x)|\leq w_2(x)}(f_2/c + (\operatorname{div} p^k - q_1^{k+1}(x) - u^k/c)) ; \tag{28}$$

3. Optimize p^{k+1} by fixing q_1^{k+1}, q_2^{k+1} and u^k, which gives

$$p^{k+1} := \arg\min_{p\in C_\alpha} \left\|\operatorname{div} p - (q_1^{k+1} + q_2^{k+1} + u^k/c)\right\|^2 . \tag{29}$$

   It is the projection of $(q_1^{k+1} + q_2^{k+1} + u^k/c)$ to the convex set $\operatorname{div} C_\alpha$.
4. Update u^{k+1} by

$$u^{k+1} = u^k + c\,(q_1^{k+1} + q_2^{k+1} - \operatorname{div} p^{k+1}) ; \tag{30}$$

   and let $k = k + 1$, repeat until convergence.

The algorithm gives a splitting optimization framework over each dual variables q_1, q_2 and p respectively, by exploring projection to their corresponding convex set. To this end, we call it the *multiplier-based algorithm to TV-L_1 image fusion*. It explores three simple sub-steps: (27), (28) and (29) at each iteration, which properly avoids tackling the nonsmooth terms in (3) in a direct way. The substeps of (27) and (28) are easy and cheap to compute. For the projection substep (29), we can use one or a few steps of the iterative projected-gradient decent algorithm to approximately solve (29) as follows:

$$p^{i+1} = \mathbf{Proj}_{C_\alpha}\Big(p^i + \tau\nabla\big\{\operatorname{div} p^i - \big((q_1^{i+1} + q_2^{i+1}) + u^i/c\big)\big\}\Big) . \tag{31}$$

Interestingly, our experiments show that just one single step of the above iteration (31), with a proper step-size τ, is needed to make the algorithm converge! This implements the algorithm in a very fast way, mostly convergences superlinearly.

5 Experiments

We implement the algorithms in both C and CUDA GPU programming. All experiments are computed by a Windows desktop with an i7 CPU (2.67 GHz) and a Nividia Tesla C1060 GPU, unless otherwise noted. For the experiments shown in Fig. 1, 2, 3 and 4, the computation of both TV-L_2 and TV-L_1 based methods, performed on CPU, finishes within a couple of seconds, while TV-L_2 algorithm is faster than the TV-L_1 algorithm due to less complexities. By GPU implementation, the computation of both methods takes around hundreds of mili-second, depending on data, which speeds up the algorithms more than 10 times in practice; especially for the 3D fusion experiments of medical imaging.

In this section, we first fuse two binary images to show the fundamental differences between (1) and (3). Then experiments for both medical imaging and remote sensing are given for qualitive comparisons of the TV-L_2 and TV-L_1 based methods. We also demonstrate the numerical performance of both methods over 3D MRI brain image fusion.

5.1 Fusing Binary Images

Given two binary images (see the two images on the leftside of Fig. 2), i.e. $f_{1,2}(x) \in \{0, 1\}$, we computed the fused image by both two approaches: (1) and (3), where the weighted functions $w_1(x)$ and $w_2(x)$ are computed based image edges. For the TV-L_2 based method (1), we set $\alpha = 3$ and its fused result $u(x)$ is shown by the 3rd image of Fig. 2. For the TV-L_1 based method (3), we set $\alpha = 1$ and its fused result $u(x)$ is shown by the last image of Fig. 2. Clearly, the TV-L_1 based method gives the binary optimum which takes the value either 0 or 1 nearly everywhere. This is in contrast to the result of the TV-L_2 based approach.

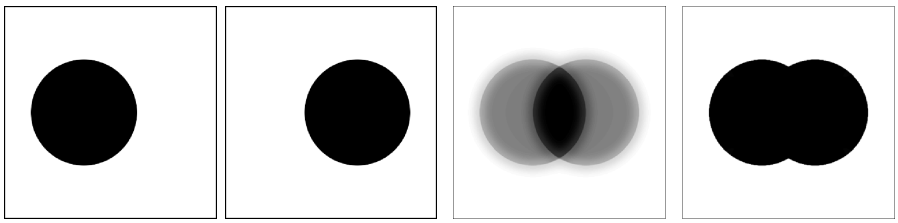

Fig. 2. Fusing binary images: (a) and (b) give the two input binary image; (c) and (d) show the results computed by the TV-L_2 and TV-L_1 based methods respectively.

5.2 Applications to Medical Imaging and Remote Sensing

Besides the fusion experiment of multi-focused images (shown in Fig. 1), we also made fusion experiments for medical imaging and remote-sensing images. Except one additional step of (27) and (28), its algorithmic scheme has the same complexities as the fast TV-L_1 method proposed in [33]. All the images are adjusted into the same grayscale range for comparisons. Fig. 3 shows the fusion experiment of medical imaging, which integrates the images from CT and MRI (see Fig. 3). The TV-L_1 based method performs visually better than the TV-L_2 based method in preserving high-contrast and details (see the enlarged image patches for comparisons). Fig. 4 shows the image fusion experiment of remote sensing, where two images from different spectral channels are fused by the studied two methods respectively. Detailed comparison of the enlarged patches (see the images at 2nd row of Fig. 4) clearly indicates better visual result by the TV-L_1 based method.

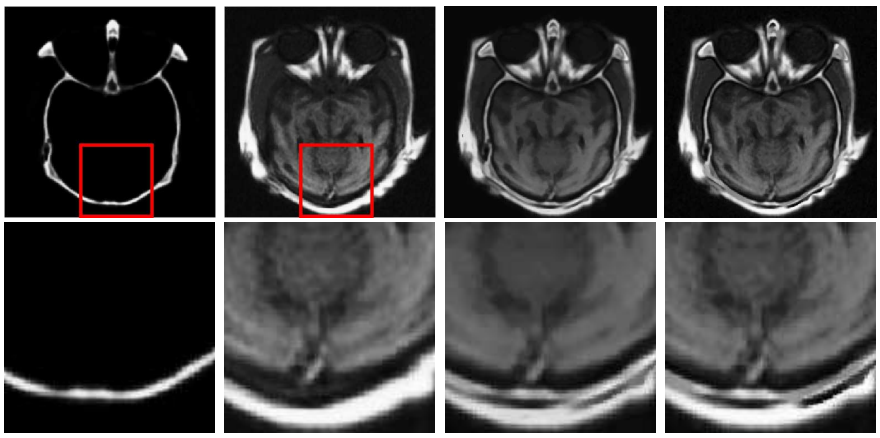

Fig. 3. Fusing medical images. **1st row:** the left two images show two input, a CT of the head and an MRI image of the head respectively. The results by TV-L_2 based method and TV-L_1 based method are given by the third and fourth images respectively. (1) and (3) respectively. **2nd row:** the left two images show the zoomed image patches cropped by the red lines on the same position of CT and MRI images respectively; the right two images show the fused results at the patched area computed by (1) and (3) respectively.

5.3 Application to 3D Medical Image Fusion

In this section, we show the numerical performance of the two proposed algorithms for 3D image-volume fusion, where the simulated T1 and T2 3D MRI volumes are used. These 3D image volumes are downloaded from the brain-web

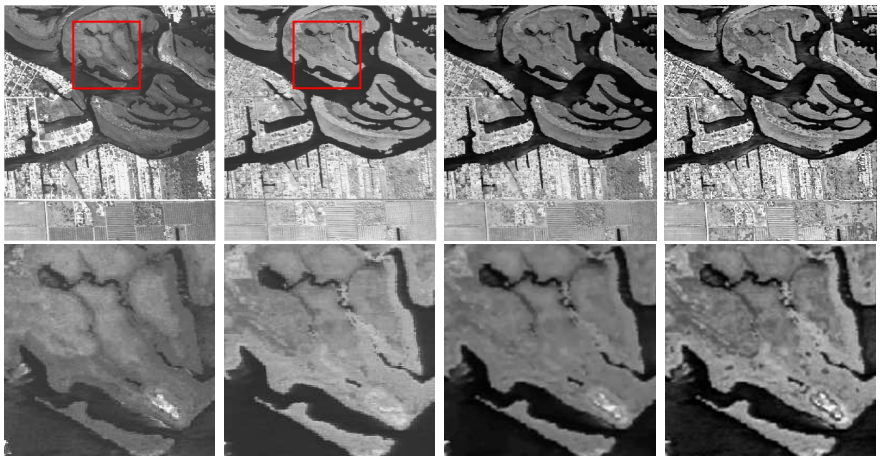

Fig. 4. Fusing images from two spectral bands. **At 1st row:** the left two images show the input images of remote sensing images from two different spectral channels; the right two images show the fused images computed by (1) and (3) respectively. **At 2nd row:** the left two images show the zoomed image patches croped by the red lines on the same position of the input images respectively; the right two images show the fused results at the patched area computed by (1) and (3) respectively.

	Computation Time (s)	Iteration to Convergence
TVL1 - GPU	7.551	122
TVL1 - CPU	61.745	122
TVL2 - GPU	0.848	15
TVL2 - CPU	35.607	15

Table 1. Computational Times and Iterations to Convergence for the Brain Image Fusion

database http://mouldy.bic.mni.mcgill.ca/brainweb/. This volume has $217 \times 181 \times 181$ equally sized voxels, each 1mm cubed. The fused 3D image volumes can provide an additional view of the patient to support clinician checks. We list the number of iterations and the computation time in table 1. The computation results are shown in Fig. 5, visulized in aggital, axial and coronal views. Clearly, the TV-L_1 based fusion method is slower than the TV-L_2 based method, but is compensated by its better visual results.

6 Conclusion and Future Directions

In this work, we consider two variational approaches to image fusion, which are related to TV-L_2 and TV-L_1 image approximation. We propose their new equivalent convex formulations in terms of primal and dual and show their resulted new image decompositions. We focus on the TV-L_1 based image fusion approach

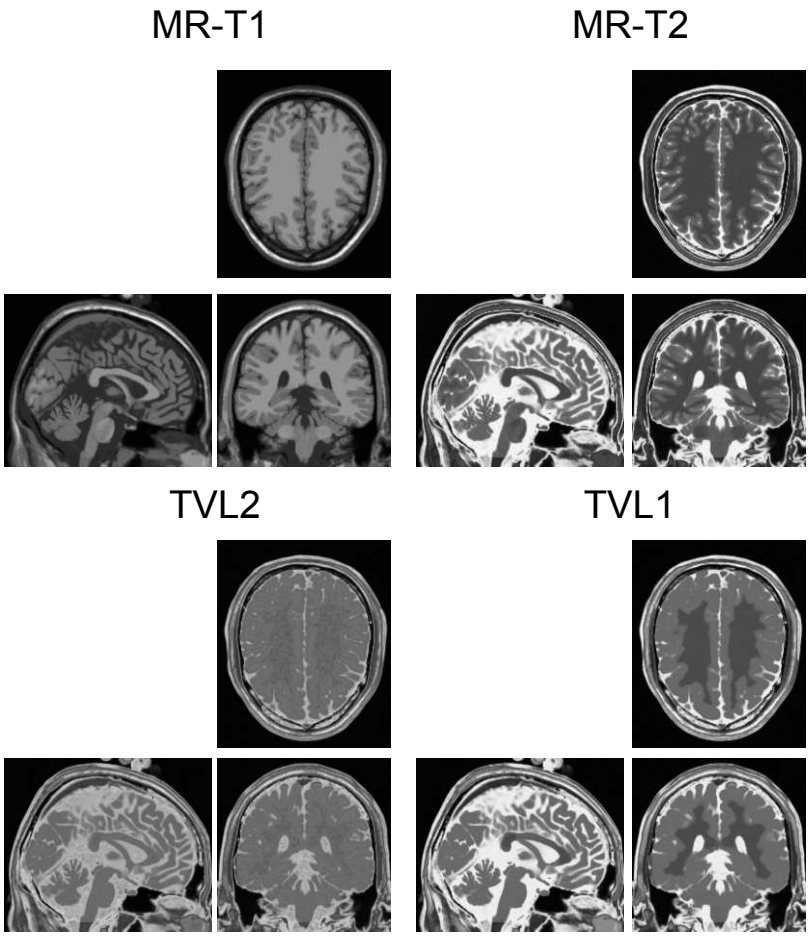

Fig. 5. Fusing 3D brain MRI image volumes (T1 and T2): all the 3D volumes are shown in saggital, axial and coronal views. **Top-left** shows the T1 volume; **Top-right** shows the T2 volume; **Bottom-left** shows the fused volume by the TV-L_2 based method; **Bottom-right** shows the fused volume by the TV-L_1 based method.

and consider fusing two discrete-valued images. In this regard, we prove that the TV-L_1 based image fusion actually gives the exact convex relaxation to its corresponding image fusion subject to the specified discrete-valued constraint, which greatly simplifies the optimization problem and results in significantly efficient solvers in numerics to the practical imaging tasks. This extends recent developments for global optimization of the discrete-constrained TV-L_1 image approximation [7, 33] to the case of image fusion.

The proposed dual models lead to fast and reliable algorithmic schemes based on the standard convex optimization. Experiments show the TV-L_1 based image fusion method outperforms over the TV-L_2 based method for preserving better contrast and more details. Further experiments of 3D medical image fusion demonstrate the numerical performance of the two proposed approaches in practice, and confirm their applicabilities to real image fusion.

References

1. B. Aiazzi, L. Alparone, S. Baronti, and A. Garzelli. Context-driven fusion of high spatial and spectral resolution images based on oversampled multiresolution analysis. *IEEE Geoscience and Remote Sensing*, 40(10):2300–2312, 2002.
2. Jean-François Aujol, Guy Gilboa, Tony F. Chan, and Stanley Osher. Structure-texture image decomposition - modeling, algorithms, and parameter selection. *International Journal of Computer Vision*, 67(1):111–136, 2006.
3. Egil Bae, Jing Yuan Xue-Cheng Tai, and Yuri Boykov. A study on continuous max-flow and min-cut approaches part ii: Multiple linearly ordered labels. Technical report CAM-10-62, UCLA, CAM, 2010.
4. Dimitri P. Bertsekas. *Constrained optimization and Lagrange multiplier methods*. Academic Press Inc., New York, 1982.
5. Yuri Boykov, Olga Veksler, and Ramin Zabih. Fast approximate energy minimization via graph cuts. *IEEE PAMI*, 23(11):1222–1239, November 2001.
6. A. Chambolle. An algorithm for total variation minimization and applications. *Journal of Mathematical Imaging and Vision*, 20(1-2):89–97, Jan 2004.
7. Tony F. Chan and Selim Esedo$\bar{\text{g}}$lu. Aspects of total variation regularized L^1 function approximation. *SIAM J. Appl. Math.*, 65(5):1817–1837 (electronic), 2005.
8. Tony F. Chan, Selim Esedoglu, and Mila Nikolova. Algorithms for finding global minimizers of image segmentation and denoising models. *SIAM J. Appl. Math.*, 66(5):1632–1648 (electronic), 2006.
9. Tony F. Chan and Luminita A. Vese. Active contours without edges. *IEEE Transactions on Image Processing*, 10(2):266–277, 2001.
10. Asha Das and K. Revathy. A comparative analysis of image fusion techniques for remote sensed images. In *World Congress on Engineering*, pages 639–644, 2007.
11. Ivar Ekeland and Roger Téman. *Convex analysis and variational problems*. Society for Industrial and Applied Mathematics, Philadelphia, PA, USA, 1999.
12. Ky Fan. Minimax theorems. *Proc. Nat. Acad. Sci. U. S. A.*, 39:42–47, 1953.
13. Enrico. Giusti. *Minimal surfaces and functions of bounded variation*. Australian National University, Canberra, 1977.
14. Hiroshi Ishikawa. Exact optimization for markov random fields with convex priors. *IEEE PAMI*, 25:1333–1336, 2003.

15. Stefan Kluckner, Thomas Pock, and Horst Bischof. Exploiting redundancy for aerial image fusion using convex optimization. In *DAGM*, pages 303–312, 2010.
16. H. Li, B. S. Manjunath, and S. K. Mitra. Multisensor image fusion using the wavelet transform. *Graphical Models and Image Processing*, 57(3):235–245, 1995.
17. Yves Meyer. *Oscillating patterns in image processing and nonlinear evolution equations*, volume 22 of *University Lecture Series*. American Mathematical Society, Providence, RI, 2001. The fifteenth Dean Jacqueline B. Lewis memorial lectures.
18. Jorge Nez, Xavier Otazu, Octavi Fors, Albert Prades, Vicenc Pal'a, and Roman Arbiol. Multiresolution-based image fusion with additive wavelet decomposition. *IEEE Trans. On Geoscience And Remote Sensing*, 37(3):1204–1211, May 1999.
19. S. Osher, M. Burger, D. Goldfarb, J. Xu, and W. Yin. An iterative regularization method for total variation-based image restoration. *Multiscale Modeling and Simulation*, 4(2):460–489, 2006.
20. Gonzalo Pajares and Jesús Manuel de la Cruz. A wavelet-based image fusion tutorial. *Pattern Recognition*, 37(9):1855–1872, 2004.
21. Gemma Piella. Image fusion for enhanced visualization: A variational approach. *International Journal of Computer Vision*, 83(1):1–11, 2009.
22. R. T. Rockafellar. Augmented Lagrangians and applications of the proximal point algorithm in convex programming. *Math. of Oper. Res.*, 1:97–116, 1976.
23. L. Rudin, S. Osher, and E. Fatemi. Nonlinear total variation based noise removal algorithms. *Physica D*, 60(1-4):259–268, 1992.
24. Robert A. Schowengerdt. *Remote Sensing: Models and Methods for Image Processing*. Elsevier, 3rd edition, 2007.
25. Moon-Jun Sohn, Dong-Joon Lee, Sang Won Yoon, Hye Ran Lee, and Yoon Joon Hwang. The effective application of segmental image fusion in spinal radiosurgery for improved targeting of spinal tumours. *Acta Neurochir*, 151:231–238, 2009.
26. Wei-Wei Wang, Peng-Lang Shui, and Xiang-Chu Feng. Variational models for fusion and denoising of multifocus images. *IEEE Signal Processing Letters*, 15:65–68, 2008.
27. Zhijun Wang, D. Ziou, C. Armenakis, D. Li, and Qingquan Li. A comparative analysis of image fusion methods. *IEEE Geo. and Res.*, 43(6):1391–1402, 2005.
28. Chunlin Wu, Juyong Zhang, and Xue-Cheng Tai. Augmented lagrangian method for total variation restoration with non-quadratic fidelity. Technical report CAM-09-82, UCLA, CAM, 2009.
29. L. Yang, B.L.Guo, and W.Ni. Multimodality medical image fusion based on multiscale geometric analysis of contourlet transform. *Neurocomputing*, 72:203–211, 2008.
30. Wotao Yin, Donald Goldfarb, and Stanley Osher. The total variation regularized l^1 model for multiscale decomposition. *Multiscale Modeling and Simulation*, 6(1):190–211, 2007.
31. J. Yuan, E. Bae, X.C. Tai, and Y. Boykov. A continuous max-flow approach to Potts model. In *ECCV 2010*.
32. Jing Yuan, Egil Bae, and Xue-Cheng Tai. A study on continuous max-flow and min-cut approaches. In *CVPR 2010*, pages 2217–2224, 2010.
33. Jing Yuan, Juan Shi, and Xue-Cheng Tai. A convex and exact approach to discrete constrained tv-l1 image approximation. Technical Report CAM-10-51, UCLA, CAM, 2010.